Gapless MoS_2 allotrope possessing both massless Dirac and heavy fermions

Weifeng Li,[1] Meng Guo,[2] Gang Zhang,[1,*] and Yong-Wei Zhang[1,†]
[1]*Institute of High Performance Computing, A*STAR, 138632 Singapore*
[2]*National Supercomputer Center in Jinan, Jinan 250101, P. R. China*
(Received 22 January 2014; revised manuscript received 17 April 2014; published 5 May 2014)

MoS_2, a member of transition metal dichalcogenides (TMDs), has recently emerged as an interesting two-dimensional material due to its unique mechanical, thermal, electronic and optical properties. Unlike graphene which possesses massless Dirac fermions with ultrahigh electron mobility, monolayer MoS_2 is a direct band gap semiconductor. An interesting question arises: Can monolayer MoS_2 also possess massless Dirac fermions with ultrahigh electron mobility? Here, using first-principles calculations, we show that a monolayer MoS_2 allotrope, which consists of repeated square-octagon rings (abbreviated as so-MoS_2 to distinguish it from the normal hexagonal lattice, h-MoS_2) possesses both massless Dirac fermions and heavy fermions. Distinct from the p-orbital Dirac fermions of graphene, the Dirac fermions of so-MoS_2 are d electrons and possess a Fermi velocity comparable to that of graphene. The Dirac cone structure in so-MoS_2 demonstrated here greatly enriches our understanding on the physical properties of TMDs and opens up possibilities for developing high-performance electronic or spintronic devices.

DOI: 10.1103/PhysRevB.89.205402 PACS number(s): 73.63.−b, 73.22.Pr

I. INTRODUCTION

One of the exceptional physical properties of graphene is the so-called Dirac cone structure [1]. In reciprocal space, the valence and conduction bands of graphene, which follow a linear dispersion relation confined to two dimensions, meet at a single point (called the Dirac point) at the Fermi level (E_F). This peculiar band structure results in an extremely high charge-carrier mobility in the form of massless Dirac fermions, and also many other interesting phenomena, ranging from the formation of conducting edge states in topological insulators to the quantum spin Hall effect due to spin-orbit coupling [1–5]. Since then, a great deal of effort has been made to search for new materials that also possess a Dirac cone structure. Apart from graphene, Dirac cones were also reported in several graphene derivatives [6–9] such as silicene and hexagonal germanium and their hybrids [2,10,11]. Common features of these two-dimensional (2D) Dirac systems are (1) a honeycomb lattice structure, and (2) sp^2 hybridized orbitals near E_F from group IV elements. It is commonly believed that the formation of a Dirac cone arises from the strong interplay between electronic and structural properties. For all the known 2D Dirac systems, the three pear-shaped lobes of the sp^2 hybridized orbitals are always in steric compatibility with the honeycomb topology, with no exception.

In recent years, monolayer MoS_2, a member of transition metal dichalcogenides (TMDs), has emerged as one of the most interesting 2D materials [12]. Monolayer MoS_2 has a planar hexagonal lattice similar to that of graphene, but its frontier orbitals are dominated by d electrons. In contrast to graphene, a monolayer MoS_2 sheet is a semiconductor with no Dirac cone. Although the allotropes of graphene have been studied extensively [6,7,13], the allotropes of monolayer MoS_2 have not been explored. Then, a couple of interesting questions arise: Is there any stable allotrope of monolayer MoS_2? If yes, does it possess a Dirac cone electronic structure?

Inspired by recent theoretical and experimental studies of grain boundary atomic structures of monolayer MoS_2 [14–16], we first construct a monolayer MoS_2 allotrope with a square crystal lattice. We then reveal that this monolayer crystal possesses a nontrivial Dirac cone with massless d electrons. Finally, we analyze the energetics and phonon spectra to prove that this material is structurally stable. This is the demonstration of Dirac fermions in a monolayer crystal beyond the group IV elements and honeycomb lattice symmetry.

II. CALCULATION METHODS

All the calculations were performed using Vienna ab initio simulation package (VASP) [17,18]. Projector-augmented-wave (PAW) potentials [19] were used to take into account the electron-ion interactions, while the electron exchange-correlation interactions were treated using the generalized gradient approximation (GGA) [20] in the Perdew–Burke–Ernzerhof scheme. A plane-wave cutoff of 500 eV was used for all the calculations. The same DFT method was used to predict the electronic structures of several monolayer materials, such as graphene and graphyne [6,8,21], silicene, hexagonal germanium, and their hybrids [10,11,22], and reasonable predictions have been obtained, demonstrating the applicability of the method to this class of materials. All atomic positions and lattice vectors were fully optimized by using a conjugate gradient algorithm to obtain the ground-state configuration. A vacuum layer of 25 Å was kept between so-MoS_2 sheets in the c direction to avoid mirror interactions. Atomic relaxation was performed at extremely critical conditions: the change of total energy was less than 0.001 meV and all the Hellmann–Feynman forces on each atom were smaller than 0.0001 eV/Å, which guarantee fully relaxed structures and the accuracy for the following phonon dispersion calculation. A k-point sampling of $7 \times 7 \times 1$ was used for the structure relaxation, while a denser mesh of $45 \times 45 \times 1$ was used to calculate density of states (DOS) and band structures.

*zhangg@ihpc.a-star.edu.sg
†zhangyw@ihpc.a-star.edu.sg

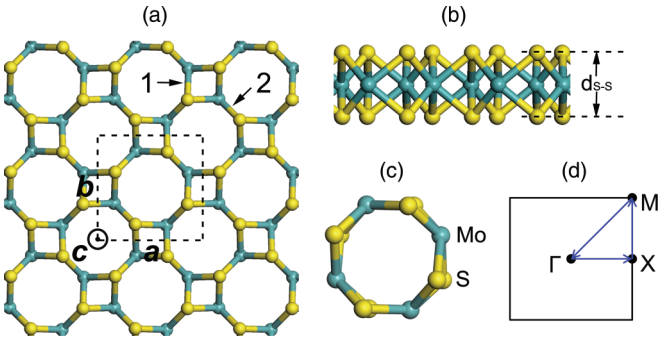

FIG. 1. (Color online) (a) Top view and (b) side view of so-MoS_2. The dashed-line square and bold italic text ***a***, ***b*** and ***c*** in panel (a) indicate the primitive cell, which is also highlighted in panel (c) and the three lattice-vector directions, respectively. (d) The first Brillouin zone of so-MoS_2 with letters designating special points and the lines for band-structure calculation.

Because the structural stability of the 2D structure is a critical issue, we calculated the phonon spectra of so-MoS_2. The phonon dispersion was first calculated using the PHON program [23] based on the finite displacement method from VASP calculations. A supercell containing 3×3 of the primitive cell was used to calculate the force constant matrix. According to the symmetry operations of $p4$ crystals, there are two nonequivalent atoms in the primitive cell (one Mo and one S, as shown in Fig. 1(a) and the displacements along the ***a*** axis and ***c*** axis were considered for each atom (with displacement of 0.04 Å). The forces on all the atoms in the supercell for each displacement were calculated with VASP with a k-point sampling of $9 \times 9 \times 1$. The phonon dispersion was further checked with the CASTEP modulus in MATERIAL STUDIO [24], based on the linear-response method. A plane-wave cutoff of 650 eV was used for the calculations.

III. RESULTS AND DISCUSSION

A. Lattice structure of so-MoS_2

In the commonly studied monolayer MoS_2; that is, h-MoS_2, the transition-metal atoms are located in one sublattice, which is sandwiched by two superimposed chalcogenide atomic layers in the other sublattice. In addition to six-membered rings, four- and eight-membered rings consisting entirely of hetero-elemental bonds (S-Mo) were also found at the grain boundaries in monolayer h-MoS_2 [15]. Inspired by these stable grain-boundary structures, we construct a monolayer MoS_2 as shown in Fig. 1(a) by repeating the square-octagon pairs in a square lattice (abbreviated so-MoS_2 to distinguish from the normal hexagonal lattice, h-MoS_2). The primitive cell is square with $p4$ symmetry, containing four Mo and eight S atoms.

The optimized structure of so-MoS_2 has a lattice constant of 6.36 Å. The thickness of the monolayer [measured from S in the top layer to S in the bottom layer as illustrated in Fig. 1(b)] is 3.12 Å, similar to that of h-MoS_2 which is 3.13 Å. There are structural distortions in so-MoS_2 because of the square-octagon topology: the Mo-S bonds that constitute the square [labelled 1 in Fig. 1(a)] are stretched to 2.46 Å, while the Mo-S bonds that link the squares [labelled 2 in Fig. 1(a)] are compressed to a length of 2.39 Å. As a comparison, the Mo-S bond in h-MoS_2 is homogeneously 2.42 Å.

B. Electronic band structure and frontier orbitals

A representative three-dimensional (3D) plot that reveals the shape of the conduction and valence bands is shown in Fig. 2(a). It is exciting to find that the lower cone (from the valence band) possesses a linear dispersion relation near the Dirac point, indicating massless Dirac fermions. The electronic band structures of so-MoS_2 are shown in Fig. 2(b). It is seen that the valence band, conduction band, and conduction band +1 (VB, CB, and CB + 1) approach the Γ point at E_F. The slopes of VB are −16.0 eV Å (X to Γ) and +15.4 eV Å (M to Γ), respectively. The upper cone (from CB + 1) locates 3 meV above E_F at the Γ point. The slopes of the CB + 1 branch are +15.6 eV Å (X to Γ) and −15.5 eV Å (M to Γ), respectively. We also calculate the Fermi velocity (v_F) of the Dirac fermions by using $v_F = E(k)/(\hbar k)$, which is about 2.3–2.4 $\times 10^6$ m/s, comparable to that of graphene [9,25], but an order of magnitude higher than that of hexagonal silicene and germanium monolayers [2,11]. The CB deviates from the linear slope and is flattened, indicating the coexistence of heavy fermions. The effective mass of the heavy fermion can

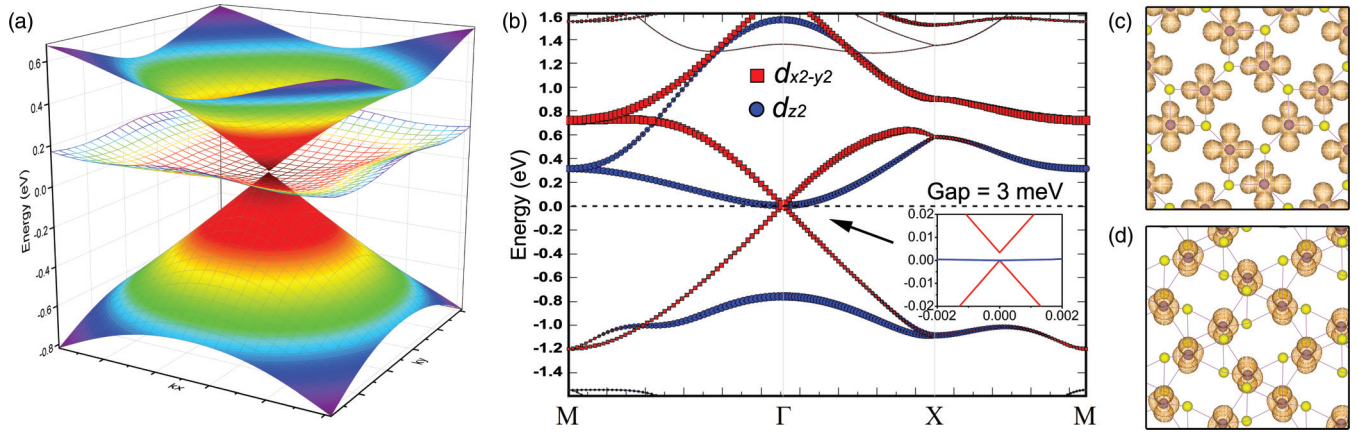

FIG. 2. (Color online) (a) Dirac cone formed in the vicinity of the Dirac point. (b) Electronic band structures of so-MoS_2. (c), (d) Charge-density plots of the $d_{x2\text{-}y2}$ and d_{z2} orbitals of Mo, respectively (electron orbital isosurface level of 0.01 $Å^{-3}$).

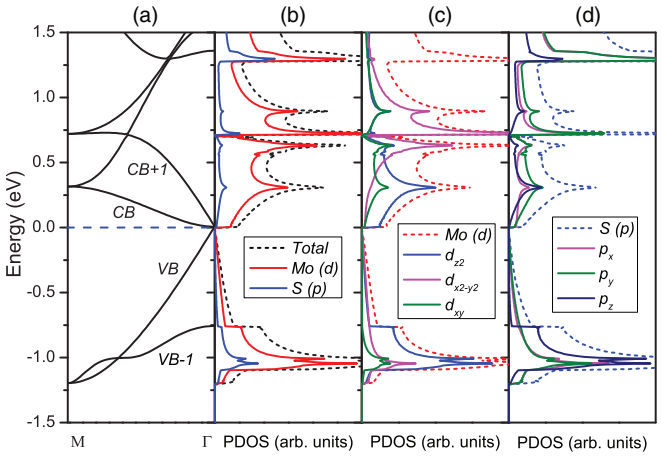

FIG. 3. (Color online) (a) Band structures of so-MoS_2 from M to Γ. (b) Total DOS and projections on Mo d orbitals and S p orbitals. (c) PDOS of Mo d orbitals and projections on d_{z2}, d_{x2-y2}, and d_{xy}. (d) PDOS of S p orbitals and projections on p_x, p_y, and p_z.

be estimated using the following equation at the CB minimum:

$$m^* = \frac{\hbar^2}{\partial^2 E(k)/\partial k^2}. \quad (1)$$

Our calculations show that the effective masses are $1.11m_e$ (X to Γ) and $1.78m_e$ (M to Γ), respectively. The complicity of these two unoccupied bands contributes to a moderate level of density of state (DOS) just above E_F, while the DOS just below E_F is zero, as shown in Fig. 3(b). This implies that, above zero temperature, excitations of electrons to CB and CB + 1 are able to cause a high charge-carrier density as well as extremely high carrier mobility. Hence a better conductivity than graphene is expected due to its zero carrier density at E_F.

It is well known that, in TMDs, the frontier orbitals mainly originate from the d orbitals of transition metals, with weak contributions from the p orbitals of chalcogen atoms [26–30]. In h-MoS_2, d_{xy} and d_{x2-y2} orbitals of Mo are doubly degenerated in energy, while d_{yz} and d_{xz} are also doubly degenerated and d_{z2} is singly degenerated. For S atoms, p_x and p_y are degenerated. From hexagonal lattices ($p6m$ symmetry) to square lattices ($p4$ symmetry), some structure symmetries are lost, as well as the electron orbital degeneracies. These changes can be clearly observed from the orbital projected density of states (PDOS), as illustrated in Fig. 3. The frontier orbitals of so-MoS_2 mainly contain Mo d electrons. More specifically, the VB and CB + 1 are mainly composed of the d_{x2-y2} orbital of Mo, as shown in Fig. 3(c), whereas the CB and VB − 1 are mainly composed of the d_{z2} orbital of Mo. Charge-density plots of the four orbitals near E_F can be found in Fig. 4, where the CB + 1 and VB − 1 are contributed from nearly ideal d_{x2-y2} and d_{z2} orbitals, respectively, whereas the VB and CB are mixed orbitals (d_{x2-y2} with d_{z2}) due to their hybridization at the Γ point. Overall, the contributions from S p electrons are almost negligible.

In real space, the four pear-shaped lobes of in-plane d_{x2-y2} orbitals spread in the so-MoS_2 plane and have centers on the ***a*** and ***b*** lattice axes, as shown in Fig. 2(c), fully compatible with the square lattice symmetry. Consequently, a long-range

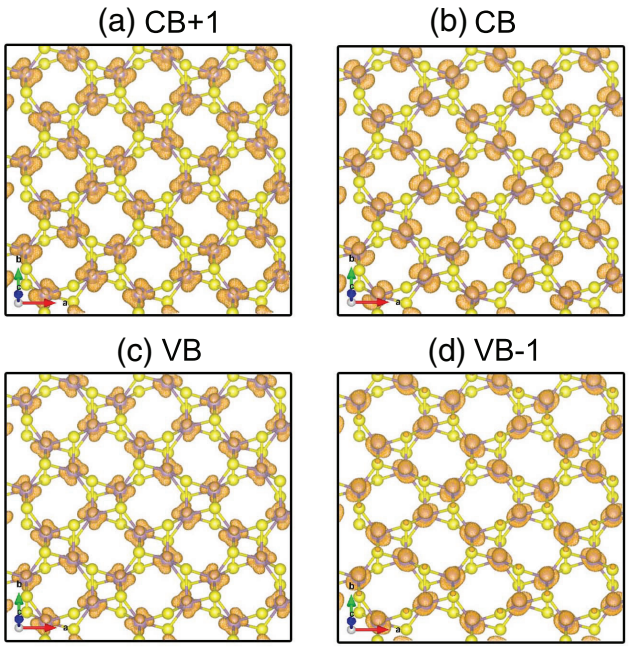

FIG. 4. (Color online) Charge-density plots of the four orbitals (electron orbital isosurface level of 0.01 $Å^{-3}$) near the Fermi level: (a) conduction band +1, (b) conduction band, (c) valence band, and (d) valence band −1.

coherence is realized between the d_{x2-y2} orbital and the square crystal lattice, leading to the formation of a Dirac cone. On the contrary, the two pear-shaped regions of out-of-plane d_{z2} orbitals are more localized, placing symmetrically on the ***c*** axis as shown in Fig. 2(d), resulting in the heavy fermions.

C. Structure stability and phonon spectrum

In order to assess the stability of the so-MoS_2-based Dirac fermion system, we first calculated the formation energy (normalized to each atom), defined as

$$E_{form} = \frac{E_{total} - n_{Mo}E_{Mo} - n_S E_S}{n_{Mo} + n_S}. \quad (2)$$

Our calculation shows that E_{form} is about −4.79 eV/atom, comparable to a value of −5.07 eV/atom for h-MoS_2, indicating that so-MoS_2 is only slightly less stable than h-MoS_2. Furthermore, we also examined the thermal stability by calculating the phonon dispersion relations, which can pinpoint the stability of materials [31]. The phonon band structures are shown in Fig. 5. The obtained phonon dispersions from two different calculation methods (small-displace method and linear-response method) agree well with each other, except that the energy degeneracy is predicted from PHON for the acoustic modes approaching Γ from M. Since there are no imaginary frequencies (negative frequencies) found in the whole phonon spectrum, the so-MoS_2 is structurally stable. A possible approach to realize so-MoS_2 is to use specific substrates, similar to the strategy used to grow a hexagonal hafnium (Hf) layer on an Ir(111) surface [32] and silicene on Ag(111) [33,34].

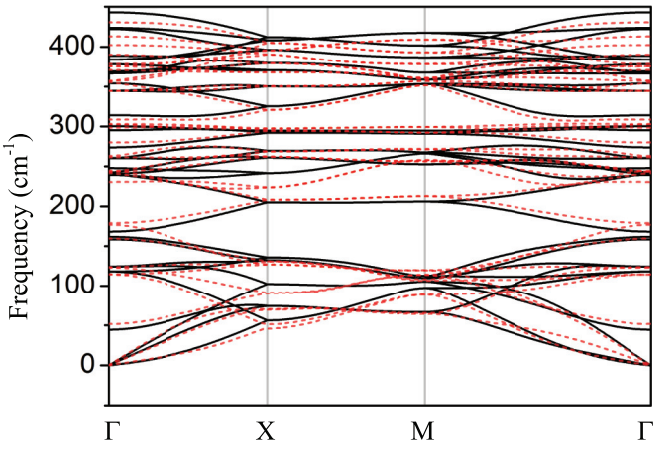

FIG. 5. (Color online) Phonon band structures of so-MoS_2 obtained from small-displacement method (black solid lines) and linear-response method (red dashed lines) along highly symmetric q directions in the Brillouin zone.

It is seen that, originating from the Γ point, there are three zero-frequency acoustic branches. The lowest branch shows a quadratic energy dispersion relation in q, corresponding to the out-of-plane displacement (ZA mode). The other two branches display a linear q dependence around the Γ point, representing the in-plane transverse and longitudinal displacements (TA and LA modes) in two orthogonal directions, so

$$\omega_\lambda = \begin{cases} v_\lambda q, & \lambda = \text{LA,TA} \\ \alpha q^2, & \lambda = \text{ZA}, \end{cases} \tag{3}$$

where v_λ is the group velocity of branch λ. In general, the thermal conductivity of materials is predominantly contributed by these three acoustic branches, since the numbers of higher-frequency optical branches are at least one order of magnitude lower than those in the acoustic branches. As a consequence, the values of v_λ and α in Eq. (3) can be used to evaluate the thermal conductivity by the linearized phonon Boltzmann transport equation [35]. The values are summarized in Table I. The group velocities for LA and TA branches are 713.34 m/s and 546.62 m/s, respectively, and $\alpha = 8.92 \times 10^{-8}$ m^2/s for the ZA branch, which is obtained from the small-displacement calculation. The linear-response calculation predicted quantitatively consistent group velocities, which are 753.82 m/s and 505.36 m/s for LA and TA branches, respectively. In addition, this calculation also predicted a similar value, 6.61×10^{-8} m^2/s, for α. The group velocities and α of so-MoS_2 are slightly lower than those of h-MoS_2, which are 1029.22 (LA) and 624.51 (TA) m/s, and 10.13×10^{-8} m^2/s for the ZA branch in our present study. The values of v_{LA} and v_{TA} of h-MoS_2 are close to those predicted from a previous first-principles calculation [36].

TABLE I. Phonon group velocity v at long-wavelength limit and α of three acoustic modes of so-MoS_2 and h-MoS_2 with small-displacement method. The values in the brackets are calculated with the linear-response method.

Materials	v_{LA} (m/s)	v_{TA} (m/s)	α_{ZA} (10^{-8} m^2/s)
so-MoS_2	713.34 (753.82)	546.62 (505.36)	8.92 (6.61)
h-MoS_2	1029.22	624.51	10.13
h-MoS_2 [36]	1108.8	693.5	

IV. CONCLUSION

To conclude, from first-principles calculations, the Dirac cone characteristic is observed in the electronic band structure of a member of the TMD family: a MoS_2 allotrope. This is the demonstration of massless Dirac fermions in a monolayer crystal beyond the group IV elements and honeycomb lattice symmetry. We find that the $d_{x2\text{-}y2}$ orbitals in so-MoS_2 form a long-range coherence with the square lattice structure, leading to the formation of Dirac fermions. We also find that the d_{z2} orbitals locate near E_F, resulting in the coexistence of heavy fermions with massless Dirac fermions in so-MoS_2. The realization of Dirac fermions in MoS_2 broadens the physical properties of the TMD family. Lattice-engineered MoS_2 can be a promising material for high-performance electronic, photonic, and spintronic devices.

ACKNOWLEDGMENTS

This work was supported by the A*STAR Computational Resource Centre through the use of its high-performance computing facilities.

[1] A. C. Neto, F. Guinea, N. Peres, K. S. Novoselov, and A. K. Geim, Rev. Mod. Phys. **81**, 109 (2009).
[2] C. C. Liu, W. Feng, and Y. Yao, Phys. Rev. Lett. **107**, 076802 (2011).
[3] M. Z. Hasan and C. L. Kane, Rev. Mod. Phys. **82**, 3045 (2010).
[4] X. L. Qi and S. C. Zhang, Phys. Today **63**(1), 33 (2010).
[5] H. Zhang, C.-X. Liu, X.-L. Qi, X. Dai, Z. Fang, and S.-C. Zhang, Nat. Phys. **5**, 438 (2009).
[6] D. Malko, C. Neiss, F. Viñes, and A. Görling, Phys. Rev. Lett. **108**, 086804 (2012).
[7] K. K. Gomes, W. Mar, W. Ko, F. Guinea, and H. C. Manoharan, Nature (London) **483**, 306 (2012).
[8] Y. Li, P. Chen, G. Zhou, J. Li, J. Wu, B.-L. Gu, S. B. Zhang, and W. Duan, Phys. Rev. Lett. **109**, 206802 (2012).
[9] C. Hwang, D. A. Siegel, S.-K. Mo, W. Regan, A. Ismach, Y. Zhang, A. Zettl, and A. Lanzara, Sci. Rep. **2**, 590 (2012).
[10] J. C. Garcia, D. B. de Lima, L. V. Assali, and J. F. Justo, J. Phys. Chem. C **115**, 13242 (2011).
[11] H. Zhou, M. Zhao, X. Zhang, W. Dong, X. Wang, H. Bu, and A. Wang, J. Phys.: Condens. Matter **25**, 395501 (2013).
[12] M. Chhowalla, H. S. Shin, G. Eda, L.-J. Li, K. P. Loh, and H. Zhang, Nat. Chem. **5**, 263 (2013).
[13] L. C. Xu, R. Z. Wang, M. S. Miao, X. L. Wei, Y. P. Chen, H. Yan, W. M. Lau, L. M. Liu, and Y. M. Ma, Nanoscale **6**, 1113 (2014).
[14] S. Najmaei, Z. Liu, W. Zhou, X. Zou, G. Shi, S. Lei, B. I. Yakobson, J.-C. Idrobo, P. M. Ajayan, and J. Lou, Nat. Mater. **12**, 754 (2013).

[15] A. M. van der Zande, P. Y. Huang, D. A. Chenet, T. C. Berkelbach, Y. You, G.-H. Lee, T. F. Heinz, D. R. Reichman, D. A. Muller, and J. C. Hone, Nat. Mater. **12**, 554 (2013).
[16] Z. Zhang, X. Zou, V. H. Crespi, and B. I. Yakobson, ACS Nano **7**, 10475 (2013).
[17] G. Kresse and J. Furthmuller, Phys. Rev. B **54**, 11169 (1996).
[18] G. Kresse and J. Furthmuller, Comput. Mater. Sci. **6**, 15 (1996).
[19] P. E. Blochl, Phys. Rev. B **50**, 17953 (1994).
[20] J. P. Perdew, J. A. Chevary, S. H. Vosko, K. A. Jackson, M. R. Pederson, D. J. Singh, and C. Fiolhais, Phys. Rev. B **46**, 6671 (1992).
[21] D. Malko, C. Neiss, and A. Görling, Phys. Rev. B **86**, 045443 (2012).
[22] S. Cahangirov, M. Topsakal, E. Aktürk, H. Şahin, and S. Ciraci, Phys. Rev. Lett. **102**, 236804 (2009).
[23] D. Alfè, Comput. Phys. Commun. **180**, 2622 (2009).
[24] M. Segall, P. J. Lindan, M. Probert, C. Pickard, P. Hasnip, S. Clark, and M. Payne, J. Phys.: Condens. Matter **14**, 2717 (2002).
[25] P. Avouris, Z. Chen, and V. Perebeinos, Nat. Nanotechnol. **2**, 605 (2007).
[26] A. Kuc, N. Zibouche, and T. Heine, Phys. Rev. B **83**, 245213 (2011).
[27] Y. Ding, Y. Wang, J. Ni, L. Shi, S. Shi, and W. Tang, Physica B (Amsterdam, Neth.) **406**, 2254 (2011).
[28] D. Voss, P. Krüger, A. Mazur, and J. Pollmann, Phys. Rev. B **60**, 14311 (1999).
[29] K. Albe and A. Klein, Phys. Rev. B **66**, 073413 (2002).
[30] S. W. Han, H. Kwon, S. K. Kim, S. Ryu, W. S. Yun, D. H. Kim, J. H. Hwang, J. S. Kang, J. Baik, H. J. Shin, and S. C. Hong, Phys. Rev. B **84**, 045409 (2011).
[31] H. Peelaers, B. Partoens, and F. Peeters, Nano Lett. **9**, 107 (2009).
[32] L. Li, Y. Wang, S. Xie, X.-B. Li, Y.-Q. Wang, R. Wu, H. Sun, S. Zhang, and H.-J. Gao, Nano Lett. **13**, 4671 (2013).
[33] B. Feng, Z. Ding, S. Meng, Y. Yao, X. He, P. Cheng, L. Chen, and K. Wu, Nano Lett. **12**, 3507 (2012).
[34] P. Vogt, P. De Padova, C. Quaresima, J. Avila, E. Frantzeskakis, M. C. Asensio, A. Resta, B. Ealet, and G. Le Lay, Phys. Rev. Lett. **108**, 155501 (2012).
[35] Y. Shen, G. Xie, X. Wei, K. Zhang, M. Tang, J. Zhong, G. Zhang, and Y.-W. Zhang, J. Appl. Phys. **115**, 063507 (2014).
[36] Y. Cai, J. Lan, G. Zhang, and Y.-W. Zhang, Phys. Rev. B **89**, 035438 (2014).